UNIVERSITY OF BIRMINGHAM

Research at Birmingham

Mapping B1-induced eddy current effects near metallic structures in MR images

Vashaee, S.; Goora, F.; Britton, Melanie; Newling, B.; Balcom, B. J.

DOI:
10.1016/j.jmr.2014.10.016

License:
Other (please specify with Rights Statement)

Document Version
Peer reviewed version

Citation for published version (Harvard):
Vashaee, S, Goora, F, Britton, MM, Newling, B & Balcom, BJ 2015, 'Mapping B1-induced eddy current effects near metallic structures in MR images: a comparison of simulation and experiment', Journal of Magnetic Resonance, vol. 250, pp. 17-24. https://doi.org/10.1016/j.jmr.2014.10.016

Link to publication on Research at Birmingham portal

Publisher Rights Statement:
NOTICE: this is the author's version of a work that was accepted for publication. Changes resulting from the publishing process, such as peer review, editing, corrections, structural formatting, and other quality control mechanisms may not be reflected in this document. Changes may have been made to this work since it was submitted for publication. A definitive version was subsequently published as S. Vashaee, F. Goora, M.M. Britton, B. Newling, B.J. Balcom, Mapping B1-induced eddy current effects near metallic structures in MR images: A comparison of simulation and experiment, Journal of Magnetic Resonance (2014), doi: http://dx.doi.org/10.1016/j.jmr.2014.10.016

General rights
Unless a licence is specified above, all rights (including copyright and moral rights) in this document are retained by the authors and/or the copyright holders. The express permission of the copyright holder must be obtained for any use of this material other than for purposes permitted by law.

• Users may freely distribute the URL that is used to identify this publication.
• Users may download and/or print one copy of the publication from the University of Birmingham research portal for the purpose of private study or non-commercial research.
• User may use extracts from the document in line with the concept of 'fair dealing' under the Copyright, Designs and Patents Act 1988 (?)
• Users may not further distribute the material nor use it for the purposes of commercial gain.

Where a licence is displayed above, please note the terms and conditions of the licence govern your use of this document.

When citing, please reference the published version.

Take down policy
While the University of Birmingham exercises care and attention in making items available there are rare occasions when an item has been uploaded in error or has been deemed to be commercially or otherwise sensitive.

If you believe that this is the case for this document, please contact UBIRA@lists.bham.ac.uk providing details and we will remove access to the work immediately and investigate.

Download date: 01. Feb. 2019

Accepted Manuscript

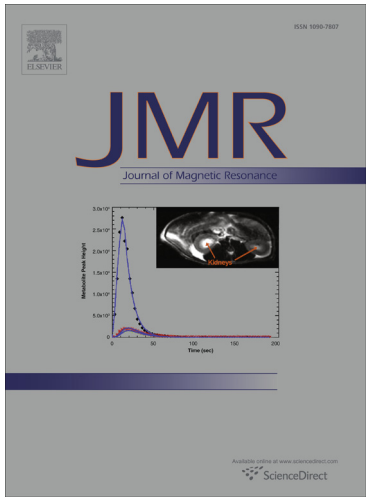

Mapping B_1-induced eddy current effects near metallic structures in MR images: A comparison of simulation and experiment

S. Vashaee, F. Goora, M.M. Britton, B. Newling, B.J. Balcom

PII: S1090-7807(14)00296-1
DOI: http://dx.doi.org/10.1016/j.jmr.2014.10.016
Reference: YJMRE 5543

To appear in: *Journal of Magnetic Resonance*

Received Date: 8 September 2014
Revised Date: 23 October 2014

Please cite this article as: S. Vashaee, F. Goora, M.M. Britton, B. Newling, B.J. Balcom, Mapping B_1-induced eddy current effects near metallic structures in MR images: A comparison of simulation and experiment, *Journal of Magnetic Resonance* (2014), doi: http://dx.doi.org/10.1016/j.jmr.2014.10.016

This is a PDF file of an unedited manuscript that has been accepted for publication. As a service to our customers we are providing this early version of the manuscript. The manuscript will undergo copyediting, typesetting, and review of the resulting proof before it is published in its final form. Please note that during the production process errors may be discovered which could affect the content, and all legal disclaimers that apply to the journal pertain.

ACCEPTED MANUSCRIPT

Mapping B_1-induced eddy current effects near metallic structures in MR images: a comparison of simulation and experiment

S. Vashaee[a], F. Goora[a], M. M. Britton[b], B. Newling[a], B.J. Balcom[a]

[a] UNB MRI Centre, Department of Physics, University of New Brunswick, Fredericton, New Brunswick, E3B 5A3, Canada.

[b] School of Chemistry, University of Birmingham, Edgbaston, Birmingham B15 2TT, UK

Corresponding Author: Prof. Bruce. J. Balcom

Telephone: 1 506 458 7938
Fax: 1 506 453 4581

Email: bjb@unb.ca

JMR-14-228Rev

Manuscript

Thursday, October 23, 2014

ACCEPTED MANUSCRIPT

ACCEPTED MANUSCRIPT

Abstract

Magnetic resonance imaging (MRI) in the presence of metallic structures is very common in medical and non-medical fields. Metallic structures cause MRI image distortions by three mechanisms: (1) static field distortion through magnetic susceptibility mismatch, (2) eddy currents induced by switched magnetic field gradients and (3) radio frequency (RF) induced eddy currents. Single point ramped imaging with T_1 enhancement (SPRITE) MRI measurements are largely immune to susceptibility and gradient induced eddy current artifacts. As a result, one can isolate the effects of metal objects on the RF field. The RF field affects both the excitation and detection of the magnetic resonance (MR) signal. This is challenging with conventional MRI methods, which cannot readily separate the three effects.

RF induced MRI artifacts were investigated experimentally at 2.4 Tesla by analyzing image distortions surrounding two geometrically identical metallic strips of aluminum and lead. The strips were immersed in agar gel doped with contrast agent and imaged employing the conical SPRITE sequence. B_1 mapping with pure phase encode SPRITE was employed to measure the B_1 field around the strips of metal. The strip geometry was chosen to mimic metal electrodes employed in electrochemistry studies.

Simulations are employed to investigate the RF field induced eddy currents in the two metallic strips. The RF simulation results are in good agreement with experimental results. Experimental and simulation results

ACCEPTED MANUSCRIPT

ACCEPTED MANUSCRIPT

show that the metal has a pronounced effect on the B_1 distribution and B_1 amplitude in the surrounding space. The electrical conductivity of the metal has a minimal effect.

Key words: metal artifacts, RF eddy current, MRI, Pure phase encode, B_1 mapping, SPRITE

ACCEPTED MANUSCRIPT

ACCEPTED MANUSCRIPT

1. Introduction

Magnetic resonance imaging (MRI) is an essential measurement and diagnostic tool in medical and non-medical fields. Metal implants like screws, hip prostheses and clips are very common clinically. The presence of metallic structures in the sample space causes image distortions. Recently the challenges of imaging near metal surfaces in electrochemical MRI studies have been investigated. MRI has enormous potential for the development of energy devices such as batteries and fuel cells, and can also be extended to investigate other electrochemical processes [1-3]. In materials science, MRI has been developed for spatially resolved analysis of fluids in porous media [4-7], MR measurements employing metal vessels at high pressure and variable temperature provide unique information about the microscopic behavior of liquids [8]. Metal vessels may lead to severe image distortions, but these distortions can be mitigated by careful choice of MRI method.

Metals produce local artifacts that distort MR images in regions close to the metal. Artifacts due to metallic objects may be caused by (1) static field magnetic susceptibility mismatch, (2) eddy currents induced by switched magnetic field gradients or (3) radio frequency (RF) field eddy currents [9-18].

Susceptibility artifacts arise from local static field (B_0) inhomogeneities caused by discontinuities in magnetic susceptibility at the boundaries of the

ACCEPTED MANUSCRIPT

metallic material and are characterized by geometric distortions in the readout direction of the image, perturbation in the selected slice and signal intensity variations. The severity of the artifact depends on the metallic object geometry, orientation with respect to the static field, the magnetic susceptibility difference, and the strength of the B_0 field [18-23]. Methods for B_0 inhomogeneity correction have been suggested in the literature [24-27]. Metallic objects generally have reduced susceptibility artifacts when their long axis is parallel to B_0 [18].

Switched magnetic field gradients and RF pulses can induce eddy currents in a metallic object, which may result in image distortion and image artifacts [20, 28-33]. In each case the varying field alters the magnetic flux through the conductive object and induces eddy currents due to Faraday's law. Lenz's law states that the eddy current flows so as to oppose the flux change inside the current path. RF eddy currents induced in the metallic object can result in B_1 enhancement or cancellation near the surface of the object [12, 17]. B_1 homogeneity in the sample space can be significantly altered. Due to the principle of reciprocity, any variation in the B_1 field has an effect both on signal excitation and signal detection. The time varying B_1 field caused by eddy currents is superimposed upon the originally applied B_1 field [16].

The severity of metal-related image distortions is determined by the pulse sequence and sequence parameters. Gradient recalled echo (GRE) methods are very sensitive to the presence of metal [34]. Intravoxel dephasing is the dominant cause of signal loss in GRE imaging, resulting in

ACCEPTED MANUSCRIPT

signal loss around the metal in the processed images. Decreasing the echo time and decreasing the voxel size will reduce the degree of intravoxel dephasing due to B_0 inhomogeneity [34]. Spin echo sequences apply refocusing RF pulses that correct for static/fixed magnetic field inhomogeneity [34]. Misregistration artifacts occur in the frequency encoding direction but not in the phase encoding direction [20, 35-37]. A technique called view angle tilting (VAT) has been shown to reduce metal related artifacts. VAT suffers from image blurring across the image field of view (FOV) and low image signal to noise ratio (SNR) [38, 40]. Single point imaging methods [35-37] with longer times for gradient stabilization can solve these problems to a significant extent. SPRITE imaging, one type of single point imaging method, may be employed to isolate B_1 related distortions since B_0 inhomogeneity, chemical shift, magnetic susceptibility, and magnetic field gradient induced eddy current artifacts are largely eliminated.

Ilott et al [9] have recently undertaken an experimental and simulation study of the electrical effects associated with lithium MRI studies of metallic lithium. Their study concentrated on the B_1 induced eddy current distribution in the lithium conductor and its spatial variation due to the skin effect.

In the current work, B_1 mapping has been undertaken to measure distortions in the B_1 field in the sample space surrounding metal conductors. We also analytically measure the local B_1 field in the sample space with a recently introduced B_1 mapping method [41]. The SPRITE MRI signal in each pixel (or voxel) is proportional to B_1^2 due to B_1 sensitivity in both

ACCEPTED MANUSCRIPT

excitation and reception. Therefore, the method is very sensitive to B_1 variation in the sample space [41].

Simulations of B_1 field induced eddy currents are also presented. The B_1 induced eddy currents result in distortion of the B_1 field in the sample space. The B_1 simulation results are in good agreement with experimental results and show the significant effects of metal on the B_1 field distribution and B_1 amplitude in surrounding space. B_1 field distortion around good conductors is largely independent of the conductivity value. Thus, the electrical conductivity of the metal has a minimal effect.

ACCEPTED MANUSCRIPT

ACCEPTED MANUSCRIPT

2. Theory

2.1. Theoretical consideration of B_1-induced artifacts

Eddy currents are induced in metallic structures by the time-varying magnetic field components of B_1. Faraday's law of induction explains this phenomenon. For a static conductor exposed to time varying magnetic flux:

$$EMF = -\frac{\partial \Phi}{\partial t} = -\frac{\partial}{\partial} \int_S \vec{B}_1 \cdot \vec{n}\, ds \qquad [1]$$

where *EMF* is the induced electromotive force due to changing flux Φ through a conductive object. $\vec{B}_1$ is the magnetic field applied for excitation and $\vec{n}$ is the normal vector perpendicular to the surface S. The induced electromotive force causes an electrical current to flow in the conductor. The induced currents, according to Lenz's law, produce local time-varying magnetic fields and as a result, the uniformity of $\vec{B}_1$ in the sample space will be disturbed. $\vec{B}_1$ distortion may result in a higher or lower amplitude of $\vec{B}_1$ locally around a metallic object, which increases or decreases the local excitation flip angle. By the principle of reciprocity, the local RF artifacts are compounded by altered receive sensitivity of the MR coil [12].

The change in transmit and receive sensitivity due to the presence of a metallic structure, assuming linear RF polarization, can be understood by

ACCEPTED MANUSCRIPT

considering a simple circuit model [12]. When current I, at frequency ω_0 is applied to a RF probe, the total effective magnetic field, B_1 (transverse to B_0), produced by the RF coil in the presence of the metallic structure is given by:

$$B(\vec{r}) = I\left[B_{1,app}(\vec{r}) + \frac{M}{Z_{metal}} B_{1,ind}(\vec{r})\right] \quad [2]$$

where $B_{1,app}$ is the transverse field per unit current applied by the RF coil in the absence of the metallic structure and $B_{1,ind}$ is the transverse field induced per unit current in the metallic structure. Only the transverse components will be considered because they are involved in exerting a torque on the net magnetic moment [12]. M is the mutual inductance between the RF coil and the metallic structure and Z_{metal} is the total impedance of the metallic structure. Z_{metal} is split into R_{metal} (resistance) and $i\omega_0 L_{metal}$ (reactance), ignoring the small capacitance. In calculating the transmit sensitivity, one should be concerned solely by the magnitude of B_1. Any phase variation will be exactly cancelled in receive mode, provided the same RF coil is employed for transmission and reception [12, 17].

The fractional changes in transmit and receive sensitivity of the RF coil, θ_{TS} and θ_{RS} [12], because of the presence of a metallic structure, are:

ACCEPTED MANUSCRIPT

$$\theta = \theta_{TS}(\vec{r}) = \theta_{RS}(\vec{r}) = \frac{\left| B_{1,app}(\vec{r}) + \frac{M}{Z_{metal}} B_{1,ind}(\vec{r}) \right|}{\left| B_{1,app}(\vec{r}) \right|} \quad [3]$$

Equation [3] can be simplified as:

$$\theta = 1 + \left| \frac{M}{Z_{metal}} \left(\frac{B_{1,ind}(\vec{r})}{B_{1,app}(\vec{r})} \right) \right| \quad [4]$$

in which, $Z_{metal} = R_{metal} + i\omega_0 L_{metal}$. The term $\frac{M}{Z_{metal}}$ is dependent upon the electrical parameters of the metallic structure and M would normally include a geometrical factor. At high frequency, $\omega_0 L_{metal}$ is much greater than R_{metal} [17], which contributes only 0.5% to the overall impedance, so the resistive term can be ignored. Dominant terms therefore only depend on metal geometry and are independent of the metal's conductivity σ_{metal}, which has an effect only through $R_{metal} \propto {}^{1}/_{\sigma_{metal}}$. The induced field, $B_{1,ind}$ of Eq.

ACCEPTED MANUSCRIPT

ACCEPTED MANUSCRIPT

4 is geometry dependent and can be calculated by applying the Biot-Savart law [12] (assuming quasi-static conditions).

2.2. Electromagnetic field analysis

A linearly polarized RF field travelling in a given direction may be expressed as:

$$\vec{\nabla}^2 H_y - k^2 H_y = 0 \qquad [5]$$

where H_y is the single component of the magnetic field and k is a propagation constant [42, 44]. Our magnetic field problem is effectively a plane wave travelling in a source free lossy media hence the square of the propagation constant is [42, 44]

$$k^2 = j\omega\mu(\sigma + j\omega\varepsilon) \qquad [6]$$

The propagation constant k is the sum of attenuation and phase constants, which are typically denoted as α and β, respectively (i.e.$k = \alpha + j\beta$). Rewriting Eq. 6 in terms of α and β [42]:

ACCEPTED MANUSCRIPT

ACCEPTED MANUSCRIPT

$$\alpha = \omega\sqrt{\mu\varepsilon}\left\{\frac{1}{2}\left[\sqrt{1+\left(\frac{\sigma}{\omega\varepsilon}\right)^2}-1\right]\right\}^{1/2} \quad [7]$$

$$\beta = \omega\sqrt{\mu\varepsilon}\left\{\frac{1}{2}\left[\sqrt{1+\left(\frac{\sigma}{\omega\varepsilon}\right)^2}+1\right]\right\}^{1/2} \quad [8]$$

The attenuation constant α is expressed in Neper per meter (Np/m) and shows the attenuation of the field as it propagates through a medium. The phase constant β in rad/s will determine the amount of phase shift. The distance the wave must travel in a lossy medium to reduce its value by a factor of e^{-1} is defined as the skin depth ($\delta = \frac{1}{\alpha}$).

In this work a metal strip was surrounded by a low conductivity gel. The conductivity of the metal strip is large relative to that of the gel. Hence, $(\sigma/\omega\varepsilon)^2 >> 1$ within the metal strip and Eqs. 7 and 8 are dominated by the conduction current density term. Similarly, $(\sigma/\omega\varepsilon)^2 << 1$ for the gel and Eqs. 7 and 8 are dominated by the displacement current density term. For each of these two cases, the exact forms of α and β as shown in Eqs. 7 and 8 can be approximated by simpler forms [42] as summarized in Table 1.

From these simplified terms, it is apparent that a wave travelling through a high conductivity metal is highly attenuated and does not effectively penetrate the conductor while experiencing rapid phase changes.

ACCEPTED MANUSCRIPT

In contrast, a wave travelling through the low conductivity gel is not significantly attenuated and does effectively penetrate it while experiencing moderate phase changes.

Solutions to Eq. 5 are not readily determined analytically. We have therefore resorted to numerical simulation in order to calculate RF magnetic field distributions in and around the sample space. In electromagnetic simulations, it is natural to employ H, since permeability and susceptibility effects may be determined from H. However, since B contains induced magnetization as well as the direct effect of H, it is the appropriate quantity to use in MR of finite permeability materials [44].

2.3. B_1 mapping around metallic structures

A new technique for B_1 mapping was employed to map B_1 around the objects of interest [41].

Practical measurement of the local B_1 proceeds via Eq. 9 by incrementing t_{pulse}, the excitation pulse duration, in successive images while maintaining the low flip angle limit [41]. Plotting local signal versus t_{pulse} permits determination of B_1 via the slope in each pixel or voxel.

$$S_{local}(\vec{r}) = \kappa \rho_0(\vec{r}) \exp(-\frac{t_p}{T_2^*}) \gamma B_1^2(\vec{r}) t_{pulse} \qquad [9$$

ACCEPTED MANUSCRIPT

ACCEPTED MANUSCRIPT

S_{local} is a unitless signal intensity in image space and κ is a constant of proportionality. ρ_0 is measured in grams of ^1H per unit volume material at any point $\vec{r}$, t_p is the phase encoding time between RF excitation and signal reception and T_2^* is the effective spin-spin relaxation time. For $t_p << T_2^*$, the exponential term may be neglected. B_1 is the component of the RF field produced in the transverse plane and γ is the gyromagnetic ratio [41].

ACCEPTED MANUSCRIPT

ACCEPTED MANUSCRIPT

4. Experimental

MRI experiments were performed on a Tecmag (Houston, TX) Apollo console equipped with a Nalorac (Martinez, CA) 2.4 T 32 cm i.d. horizontal bore superconducting magnet (Nalorac Cryogenics, Martinez, CA). The RF probe was a homebuilt quadrature eight-rung birdcage 4.5 cm in diameter and 10 cm in length, driven by a 2 kW (American Microwave Technology, Brea, CA) 3445 RF amplifier. A 200 mm i.d. gradient set driven by *x*, *y* and *z* Techron (Elkhart, IN) 8710 amplifiers, provided maximum gradient strengths of 5.9 G/cm, 5.4 G/cm and 10.6 G/cm, respectively, in this work. The RF probe was employed with a single mode of excitation and reception (linear polarization of B_1).

A conical SPRITE [36] image was acquired for a uniform cylindrical vial of gel doped with 0.2 mM $GdCl_3$ enclosing a rectangular strip of aluminum (Al), which is minimum purity 95.8% (Metal Supermarkets, Mississauga, ON, Canada). The electrical parameters of Al are summarized in Table 2. The Al strip was 3 cm in length, 1 cm in width, and 2.3 mm in thickness. The gel was 4 cm in length and 4.4 cm in diameter with bulk relaxation times of $T_2^* = 2.5$ ms and $T_1 = 21$ ms. Conical SPRITE imaging sequence parameters were: FOV = $10 \times 6.5 \times 6.5$ cm^3, SW= 250000 Hz; 64 k-space points were acquired each with a phase encoding time $t_p = 100$ μs with TR = 2 ms, signal averages = 32, 90° pulse duration 33 μs with 60% RF power. The conical SPRITE pulse length was set to 4 μs, which

ACCEPTED MANUSCRIPT

corresponds to a 6.6° flip angle. The phase cycle for both the RF pulses and the receiver was $x\bar{x}y\bar{y}$. The acquisition time for each image was 1h and 17 min.

For the 3D B_1 mapping experiments, a uniform cylindrical vial of gel, doped with 0.2 mM $GdCl_3$, 6 cm in length and 3.5 cm in diameter enclosed a rectangular strip of Al, or lead (Pb), minimum purity 98% (McMaster-Carr, Elmhurst, IL). The electrical parameters of Pb are summarized in Table 2. The strips were 5.5 cm in length 8.5 mm in width and 2.3 mm in thickness. A set of 3D SPRITE images was acquired for 3D B_1 mapping [41]. Conical SPRITE [36] imaging sequence parameters were: FOV = $13\times6\times6$ cm^3, SW= 250000 Hz, 64 k-space points were acquired each with a phase encoding time of t_p = 100 μs with TR = 2 ms, signal averages = 32, 90° pulse duration 33 μs with 60% RF power. The conical SPRITE RF pulse length was set to 3 μs, 3.5 μs, 4 μs, 4.5 μs, 5 μs, and 5.5 μs. The shortest and longest pulse durations are equal to 5° and 8° flip angles, respectively. The phase cycle for both the RF pulses and the receiver was $x\bar{x}y\bar{y}$. The acquisition time for each image was 1h and 17 min.

The Acciss, Unisort and Unifit processing packages, developed in the IDL (EXELIS, Boulder, CO) programming environment by the UNB MRI Centre were employed for image reconstruction, display and signal intensity mapping.

CST Microwave Studio (Framingham, MA), a finite element analysis software [45], was employed for the RF eddy current simulations. CST Microwave Studio is an electromagnetic field analysis program that can calculate eddy currents and resulting magnetic fields. As input parameters,

ACCEPTED MANUSCRIPT

the shape of the object, permeability, permittivity, electrical conductivity, and RF field frequency are given. As output parameters, CST provides the spatial distribution of the magnetic field intensity $\vec{H}$ along with induced current distributions $\vec{J}$ on conductive structures. In the electromagnetic simulation, the space was divided into many small mesh elements. The resulting mesh was generated such that regions of interest are meshed to a finer degree than those of less interest [28]. The number of mesh cells impacts the accuracy of the solution as well as the simulation run time. The simulations were completed using a PC with a 2.66 GHz Intel Core i7-M620 CPU with 8 GB of RAM installed.

ACCEPTED MANUSCRIPT

ACCEPTED MANUSCRIPT

5. Results and Discussion

The dimensions and orientations of the metal strips, employed in two different experimental geometries, are illustrated in Fig. 1. Figs. 1(a) and 1(b) illustrate the first geometry in which the surface of the metal strip is perpendicular to the B_1 field but parallel to B_0. *x, y*, and *z* are the laboratory frame of reference which correspond to our imaging (gradient) axes. Note that the B_1 field direction of the birdcage probe employed is not aligned with the laboratory axes. It makes a 45° angle with the *y* axis. We have chosen 45° off axis to represent the general case for a birdcage probe where the B_1 field direction is not naturally aligned with the laboratory frame of reference, unlike the case of a solenoid RF probe. The B_1 field orthogonal to the metal structure is a geometry employed in our simulations, other theoretical calculation [18], and experimental results in the literature [1].

Figs. 1(c) and 1(d) show the second experimental geometry. Fig 1(c) shows the position of the metal strip in the $GdCl_3$ doped gel. Fig 1(d) shows the B_1 and B_0 field orientations. The surface of the metal strip in this case is in the same plane as the B_1 field (*xy* plane) and perpendicular to B_0. Once again the B_1 field is oriented 45° off the *y* axis and is representative of a birdcage RF probe. The physical properties of the metal strips are reported in Table 2.

ACCEPTED MANUSCRIPT

ACCEPTED MANUSCRIPT

As stated in Section 2.2, a travelling wave penetrates the gel with little attenuation (α small) but is significantly attenuated (α large) by the metal and results in the formation of RF eddy currents. Similarly, phase changes through the gel are moderate while there are rapid changes through the metal.

We now consider experimental results with the first geometry where the surface of the metal strip is parallel to B_0 and perpendicular to B_1. Fig. 2(a) shows 2D slices of the relative B_1 field distribution (B_1/B_{1max}) (*xy* and *xz* planes) from experimental 3D B_1 maps for a uniform vial of gel doped with $GdCl_3$ enclosing a strip of Al, with orientation as shown in Fig. 1(a) and 1(b). For each orientation, five different planes, one in the centre and four displaced from the centre, are shown. The B_1 field homogeneity outside the metal strip is severely distorted with a very characteristic dipole pattern of enhanced B_1 and suppressed B_1 apparent in the transverse plane maps. B_1 artifacts will be maximized when the B_1 field is perpendicular to the surface of the strip (Eq. 1). The dipole pattern in the *xy* planes is in agreement with theory [18], experiments [1] and the simulation results that are reported below, confirming the excellent performance of our B_1 mapping method to measure B_1 in the presence of metallic structures.

Regions with enhanced and reduced B_1 in the *xy* planes are symmetric due to the symmetric shape of the metal strip. Near the eddy current, B_1 is stronger but the decrease in B_1 strength can be assumed to be inversely proportional to distance from the current source. Midway between the long

ACCEPTED MANUSCRIPT

edges of the strip, the superposition of the induced fields exactly cancels the applied field giving a net B_1 field of zero.

Asymmetry in the B_1 field alteration above and below the metal strip in the *xz* plane (longitudinal slice, right side of Fig 2(a)), is a result of the metal strip making an angle of 45° with the imaging axes (*x,y*), as shown in Fig 1(b). The central longitudinal slice is far from induced currents (along the long edges of the strip). No distortions due to $B_{1,ind}$ (the B_1 caused by induced eddy currents) will be observed above and below for the central longitudinal slice. As the *xz* planes displayed are displaced from the central plane, the region of the *xz* plane closest to the induced currents will experience greatest B_1 distortion ($B_1 = B_{1,ind} + B_{1,app}(applied\, B_1)$), while the other side further from the induced currents, experience a reduced B_1.

Fig. 2(b) shows 2D slices of the relative B_1 field distribution (B_1/B_{1max}) (*xy* and *xz* planes) from experimental 3D B_1 maps for a uniform vial of gel doped with $GdCl_3$ enclosing a strip of Pb ($\frac{\sigma_{Pb}}{\sigma_{Al}} = 1.37 \times 10^{-1}$), with orientation as shown in Fig. 1(a) and 1(b). The results are qualitatively and quantitatively the same as Fig. 2(a), suggesting that that the electrical conductivity of the metal has a minimal effect on the B_1 field in the surrounding space. In agreement with expectation (section 2.1), these results confirm that the B_1 field distortion around conductors is largely independent of the conductivity values.

We now consider the second geometry of Fig. 1 in which the surface of the metal strip is parallel to B_1 and perpendicular to B_0. Fig. 3 shows 2D slices

ACCEPTED MANUSCRIPT

(*xz* and *xy* planes) from a 3D SPRITE image of a uniform vial of gel doped with $GdCl_3$ enclosing a strip of Al, Figs. 1(c) and 1(d). The colour bar shows signal intensity in arbitrary units. For each orientation, one slice in the center of the object is shown. No B_1 distortions due to RF eddy currents were observed in the 2D *xz* slices. B_1 artifacts will be minimized when the B_1 field is parallel to the surface of the strip (EMF ≈ 0 according to Eq. 1). Note that eddy currents may still be induced in the thickness of the strip (0.23 cm), but they are negligible due to the geometry factor (surface S in Eq. 1 is very small). The results are in accordance with the theory (Eq. 1); images are free from B_1 artifacts in this case. The 2D images are free from geometrical distortion due to switched magnetic field gradients or magnetic susceptibility variations.

The *xy* transverse 2D slice does show a petal shaped signal variation in proximity to the birdcage coil struts, Fig. 3, where the B_1 field is very strong. The struts on the left and right side of the metal strip surface in the *xy* slice were the reason for the signal enhancement at top and bottom of the *xz* slice in Fig. 3 (longitudinal slice).

Since no $B_{1,ind}$ artifacts were observed for the case in which the surface of metal strip is parallel to B_1 and perpendicular to B_0, no simulations were undertaken. The $B_{1,ind}$ profoundly affects the first experimental geometry, Figs. 1(a) and 1(b). Electromagnetic simulations were undertaken to match the experimental results to the theory. Fig. 4(a) illustrates the dimensions and orientations of the metal strips employed in the simulations. The dimensions were identical to the samples studied in Fig. 2.Note that the

ACCEPTED MANUSCRIPT

simulation axes (*x',y',z'*) are different from the imaging axes (*x,y,z*). They are rotated about the *z* axis by 45°.

The direction of the applied B_1 field, $B_{1y',app,}$ was along *y'*. Fig. 4(a) shows a perspective view of the development of B_1 induced eddy currents when $B_{1y',app}$ is perpendicular to the surface of a metallic strip. According to Faraday's law of induction, Eq. 1, $B_{1y',app}$ induces an EMF which results in eddy currents. These eddy currents are concentrated at the edge of the metal strip due to the skin effect at high frequencies [18] resulting from a large attenuation constant α (theory section 2.2). The eddy currents induce a RF magnetic field $B_{1,ind}$. At the mid-point of the *z*-directed edge, $B_{1,ind}$ possesses only components in the *x'* ($B_{1x',ind}$) and *y'* ($B_{1y',ind}$) directions.

Fig. 4(b) shows a side on view of a central *x'y'* section (cross section view) of the metal strip in Fig. 4(a). The induced eddy currents $I+$ and $I-$ are into and out of the *x'y'* plane, respectively. The $B_{1,ind}$ fields are represented by the dashed lines, with a direction indicated by the arrowheads. The amplitude of the induced fields is inversely proportional to the distance from the current source in accordance with the Biot-Savart law [43]. In the proximity to the induced current, $B_{1,ind}$ effects are maximal. In areas far from the currents, the influence of $B_{1,ind}$ is minimal. At points shown by ($\times$), midway between the induced currents, the superposition of the induced fields exactly cancels out the applied field, giving a net magnetic field of zero. Knowing the direction and amplitude of $B_{1x',ind}$ and $B_{1y',ind}$, one can predict the direction and amplitude of the net B_1 field at each point in space ($B_{1i} = B_{1i,ind} + B_{1,app}, i = x', y'$).

ACCEPTED MANUSCRIPT

CST Microwave Studio was employed to simulate the spatial distribution of the magnetic field intensity $\vec{H}$ around the metal strip. $\vec{H}$ and magnetic flux density vector $\vec{B}$ are proportional by a constant of proportionality μ as shown in Eq. 9. In the simulations, the medium surrounding the electrode and gel was specified to be free space (i.e. $\mu = \mu_0$ and $\varepsilon = \varepsilon_0$).

The spatial distribution of the magnetic field intensities $H_{1x'}$ and $H_{1y'}$ in units of A/m from simulations, near and outside the modeled Al strip are shown in Figs. 5(a) and 5(b). In each figure, a central *x'y'* plane is shown. The H_{1x} and H_{1y} distributions are superposition of $H_{1x',ind}$ and $H_{1y',ind}$ with the applied H_1, $H_{1,app}$, $H_{1i} = H_{1i,ind} + H_{1,app}$, $i = x', y'$. The extent of the region in which $H_{1,ind}$ is significant is proportional to the amplitude of the RF induced eddy currents. Large amplitude eddy currents will flow at low electrical resistance (high σ) and high EMF (induced voltage), resulting from the high rate of change of the applied magnetic flux (i.e. large $\partial \vec{B}_1 / \partial t$). At high frequency, the impedance of the metal strip will be dominated by a reactive component ($Z_{metal} = R_{metal} + i\omega_0 L_{metal}$), thus the resistance of the metal, R_{metal}, will have negligible effects.

Calculations were also undertaken based on Eq. 4 for Al and Pb samples with the same geometry. Direct calculations show the effects are negligibly small (<0.008% change in M/Z_{metal}). Simulation results are in agreement with both the theory and the experimental results. Local changes of H_1 caused by the presence of metal are approximately the same for Al and Pb and are determined by the experimental geometry, which is identical. The

ACCEPTED MANUSCRIPT

electrical conductivity of the metal had negligible effects on the spatial distribution and amplitude of H_1.

Fig. 5(a) shows $H_{1x'}$, the superposition of $H_{1x',ind}$ and $H_{1,app}$ ($H_{1x'} = H_{1x',ind} + H_{1,app}$) near the Al strip. Note that $H_{1,app}$ is along the *y'* axis for this simulation so $H_{1x'}$ has the same amplitude and distribution as $H_{1x',ind}$. One can interpret the H_1 pattern as shown in Fig. 5(a) by considering the eddy current and $B_{1,\ ind}$ directions as shown in Figs. 4(a) and 4(b), respectively. $H_{1',ind}$ is directed along the $+x$ axis at the top and bottom of loops **a** and **c**, respectively. Similarly, $H_{1',ind}$ is directed along the $-x$ axis at the top and bottom of loops **b** and **d**, respectively. The maximum of $H_{1'ind}$ occurs in the region near the induced current. The amplitude of $H_{1x',ind}$ decreases as the distance from the top and bottom of each loop increases although the orientation of the field does not change.

Fig. 5(b) shows H_{1y}, which is the superposition of $H_{1y',ind}$ and $H_{1y',app}$ ($H_{1y'} = H_{1y',ind} + H_{1y',app}$) near the Al strip. One can interpret the B_1 pattern as shown in Fig. 5(b) by considering the eddy current and $B_{1,ind}$ directions as shown in Figs. 4(a) and 4(b), respectively. At the points on left side of the loops **a** and **d** as well as right sides of the loop **b** and **c**, $H_{1y'.ind}$ is positive with maximum strength near the induced currents. Further from the currents the strength will be reduced. At points on right side of the loops **a** and **d** as well as left sides of the loop **b** and **c,** $H_{1y'.ind}$ is along $-x$' with maximum strength near the induced currents. The superposition of the induced fields exactly cancels out the applied field, resulting in a net magnetic field of zero

ACCEPTED MANUSCRIPT

at the midway points labelled as (×) in Fig. 4(b), midway between the induced currents.

Simulation was also undertaken to account for the effect of the gel with an electrical conductivity of 1 S/m. No effect of gel conductivity was observed (results not shown). However, simulation for a gel with higher electrical conductivity ($\sigma > 100$ S/m) showed the gel behaving more as an RF shield. The first term on the right hand side of Eq. 17 (penetration of $\vec{H}$ into the conductor), becomes relatively large and will be large inside the gel. Due to the skin effect, the electric current mainly flows near the surface of the conductive gel.

Simulations for both the Al and the Pb strips were performed. However, the results were essentially the same for both conductors. Therefore, only the results for the Al strips are reported in this work.

Note that the B_1 field was applied perpendicular to the strip surface, as shown in Fig. 1(b), and the same RF coil was utilized for signal detection. Based on the principle of reciprocity, the signal can be detected only along $B_{1,app}$ and only the $B_{1,ind}$ components corresponding to the $B_{1,app}$ direction produce a signal. Therefore, Fig. 5(b) $H_{1y'}$ distributions ($H_{1y'} = H_{1y',ind} + H_{1y',app}$) was compared with the experimental B_1 mapping results in Fig. 6.

Figs. 6(a) and 6(b) show the central 2D slices of the relative B_1 field distribution (B_1/B_{1max}) (*xy* planes) produced from the B_1 mapping experiment for the Al and Pb strips, respectively. Figs. 6(a) and 6(b) are in a

ACCEPTED MANUSCRIPT

good agreement with Fig. 6(c) which is the normalized version of the results in Fig. 5(b). The normalized version of Fig. 5(b) was employed to facilitate comparisons of local B_1 changes between the experimental and simulation results. In Fig. 6(c) H is replaced by B/μ in which μ will be cancelled in the normalization process ($B_1/B_{1\max} = H_1/H_{1\max}$). Local B_1 changes in the experiment and simulation are in excellent qualitative and quantitative agreement.

ACCEPTED MANUSCRIPT

ACCEPTED MANUSCRIPT

6. Conclusion

B_1 induced artifacts in the presence of metal strips which mimic electrodes were investigated. The B_1 induced distortions depend on the orientation between the metal strip and the B_1 field. Two geometries were considered: (1) the surface of the metal perpendicular to B_1 and parallel to B_0 and (2) the surface of the metal parallel to B_1 and perpendicular to B_0. The first geometry lead to non-intuitive B_1 distortions, the second geometry was free from metal related B_1 artifacts.

A recently developed B_1 mapping technique was employed to measure distortions in the B_1 field in the presence of the metal strips for the first geometry. Simulations of B_1 field induced eddy currents were also undertaken. The B_1 induced eddy currents result in distortion of the B_1 field in the sample space for the first geometry. The B_1 simulation results were in good agreement with experimental results and illustrated the significant effects of the conductors on the B_1 field distribution and B_1 amplitude in surrounding space. The electrical conductivity of the metal has a negligible effect.

The results are particularly important for NMR and MRI of batteries and other electrochemical devices. Such analyses will become valuable in many applications involving battery systems. In electrochemical MRI, orienting the electrodes such that they are largely parallel to the B_1 field (B_0 field either parallel or perpendicular) will significantly reduce B_1 eddy current induced effects.

ACCEPTED MANUSCRIPT

ACCEPTED MANUSCRIPT

The objects utilized in this work were electrode-like strips of metals, but one can employ the B_1 mapping experiment and/or simulations to quantify B_1 related effects around arbitrarily complex structures.

ACCEPTED MANUSCRIPT

ACCEPTED MANUSCRIPT

6. Acknowledgements

B.J. Balcom and B. Newling thank NSERC of Canada and the Canada Chairs Programs for a Research Chair in MRI of Materials (BJB). S. Vashaee thanks R. MacGregor, B. Titus, Dr. B. MacMillan and Dr. F. Marica, for useful suggestions and technical assistance.

ACCEPTED MANUSCRIPT

ACCEPTED MANUSCRIPT

7. Figure caption

Fig 1. The dimensions and orientations of the metal strips employed in two different experimental geometries. (a) and (b) show the first case in which the surface of the metal strip was perpendicular to the B_1 field and parallel to B_0. *x, y,* and *z* are laboratory (imaging) axes. The RF probe is a birdcage probe where the B_1 field direction is not automatically aligned with lab axes *x* or *y*. (c) and (d) show the second case in which the surface of the metal strip is in the same plane as the B_1 field (*xy* plane) and perpendicular to B_0. (c) shows the position of the metal strip in the $GdCl_3$ doped gel in the second case (d) shows the directions of B_1 and B_0 with respect to the metal strip. A birdcage RF probe was employed to generate B_1.

Fig 2. (a) and (b) 2D slices of the relative B_1 field distribution (B_1/B_{1max}) in the *xy* (to the left of each figure) and *xz* (to the right) planes. 2D slices are from 3D B_1 maps for a uniform vial of gel doped with $GdCl_3$ enclosing (a) a strip of Al or (b) a strip of Pb, for the geometry in Fig. 1(a) and 1(b). For each orientation *(xy* and *xz)*, five different planes, one in the centre of the object and four displaced from centre, are shown.

Fig 3. 2D slices (*xy* and *xz* planes) from a 3D SPRITE image for a uniform vial of gel doped with $GdCl_3$ enclosing a strip of Al for the geometry in Fig. 1(c) and 1(d). The colour bar shows signal intensity in arbitrary units. For each orientation one slice in the center of the object is shown. Signal

ACCEPTED MANUSCRIPT

enhancement occurs near the end of the sample in the *xy* and *xz* 2D slices are due to the strong B_1 field near the birdcage coil struts.

Fig 4. (a) The dimensions and orientations of the metal strips employed in simulation. The simulation axes (*x',y',z'*) are different from the imaging axes (*x,y,z*). They are rotated about the *z* axis by 45°. A perspective view of the development of B_1 induced eddy currents in the metal when $B_{1y',app}$ is perpendicular to the surface of the metal strip is shown. (b) The side on view of a central *x'y'* cross section of the metal strip in (a). The induced eddy currents $I+$ and $I-$ are into and out of the *x'y'* plane, respectively. The $B_{1,ind}$ fields are represented by the dashed lines. Arrows indicate the direction of the field.

Fig 5. Magnetic field intensities $H_{1x'}$ and $H_{1y'}$ distributions from the simulation, outside the modeled Al strip for the geometry of Fig. 4(b). H is measured in units of amperes per meter (A/m). (a) shows $H_{1x'}$ which is equal to $H_{1x',ind}$ near and around the Al strip. There is no component of applied field in the *x'* direction ($H_{1x',app} = 0$) (b) shows H_{1y} which is superposition of $H_{1y',ind}$ and $H_{1y',app}$ near and around the Al strip.

Fig 6. A comparison of relative B_1 distribution ($\frac{B_1}{B_{1\max}}$) produced from the B_1 mapping experiment for the Al and Pb strips and the simulation result for the geometry in Figs. 4(b). (a) and (b) show central 2D *xy* planes of the relative B_1 field distribution for Al and Pb, respectively. (c) shows normalized versions of the H_1 simulations as shown in Figs. 5(b) for the Al

ACCEPTED MANUSCRIPT

strip. The *x'* and *y'* axes were rotated to overlap the *x* and *y* axes in order to facilitate the comparison of the simulation and experimental results. .

Table 1. Propagation constants in a good dielectric and a good conductor.

Table 2. The physical properties of the metal strips employed in the experiments and in the simulations.

ACCEPTED MANUSCRIPT

Figures:

Fig 1

(a)

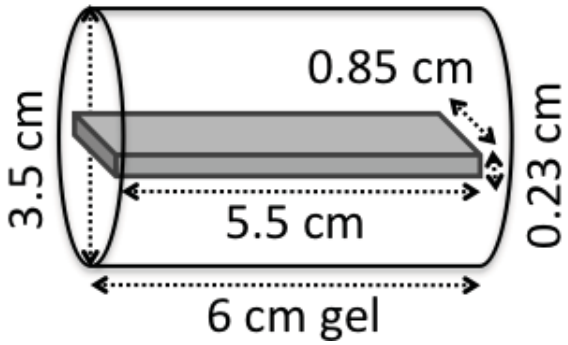

(b)

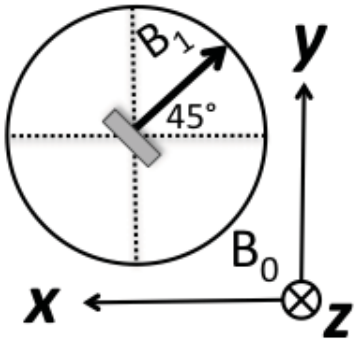

(c)

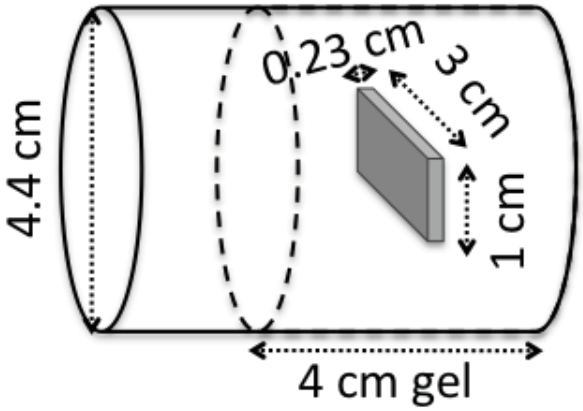

(d)

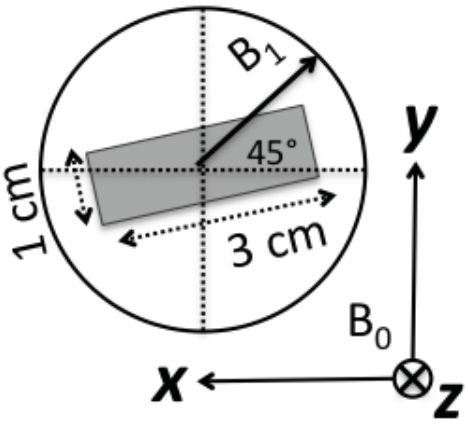

Fig 2

(a) (b)

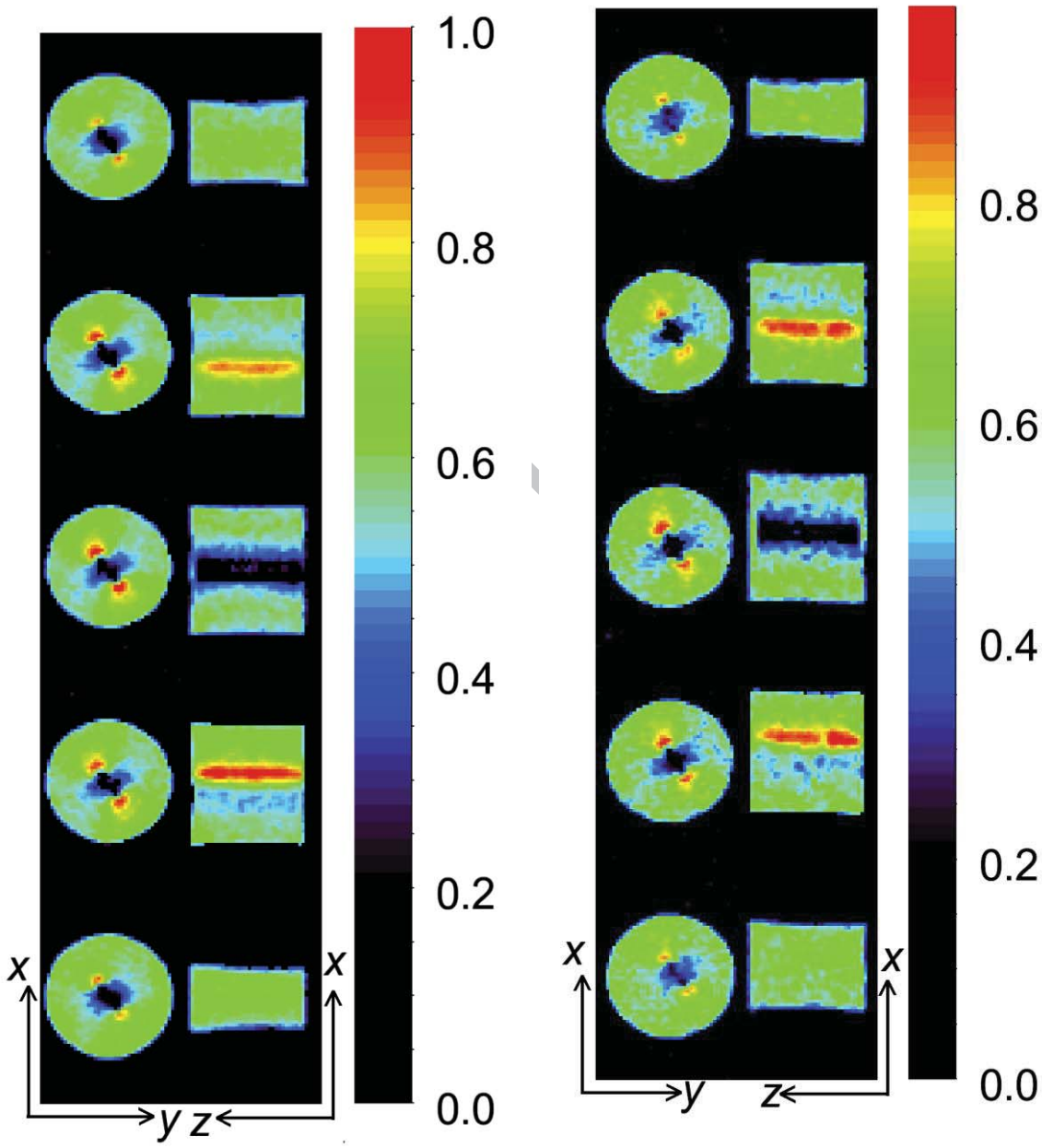

ACCEPTED MANUSCRIPT

Fig 3

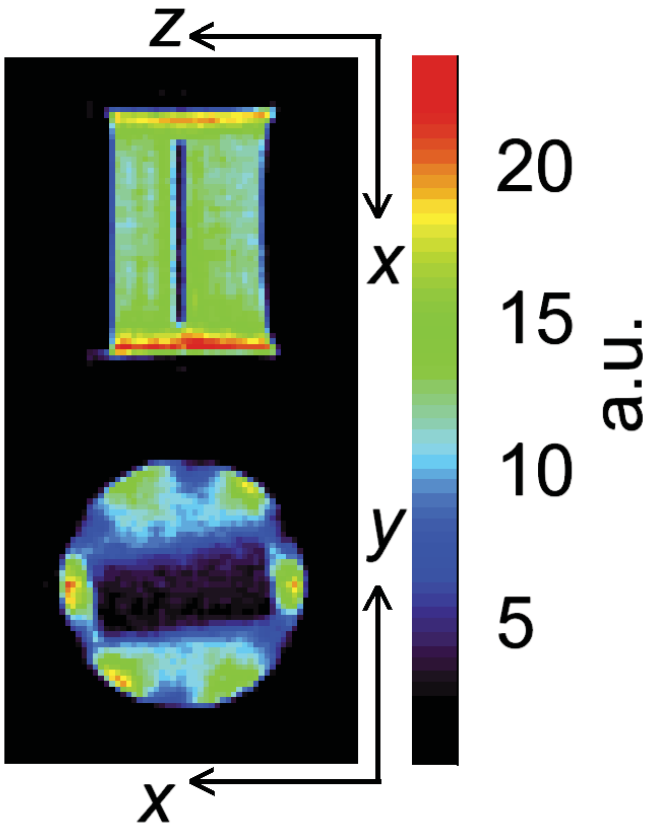

ACCEPTED MANUSCRIPT

Fig 4

(a)

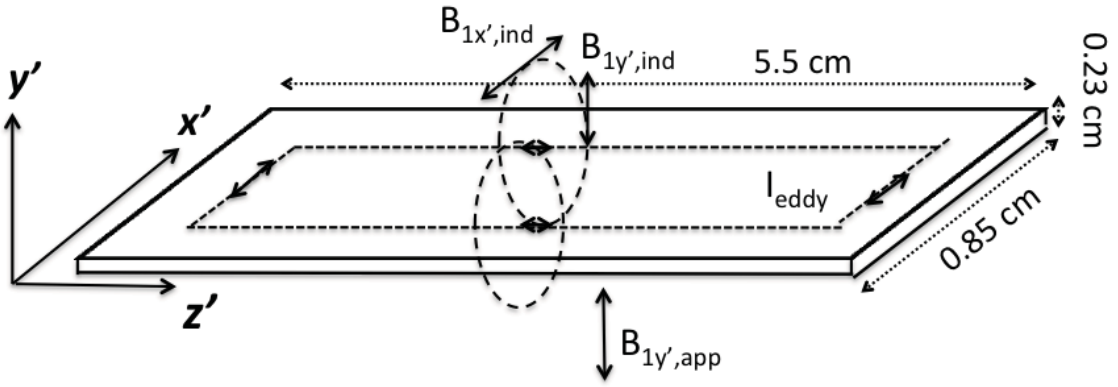

(b)

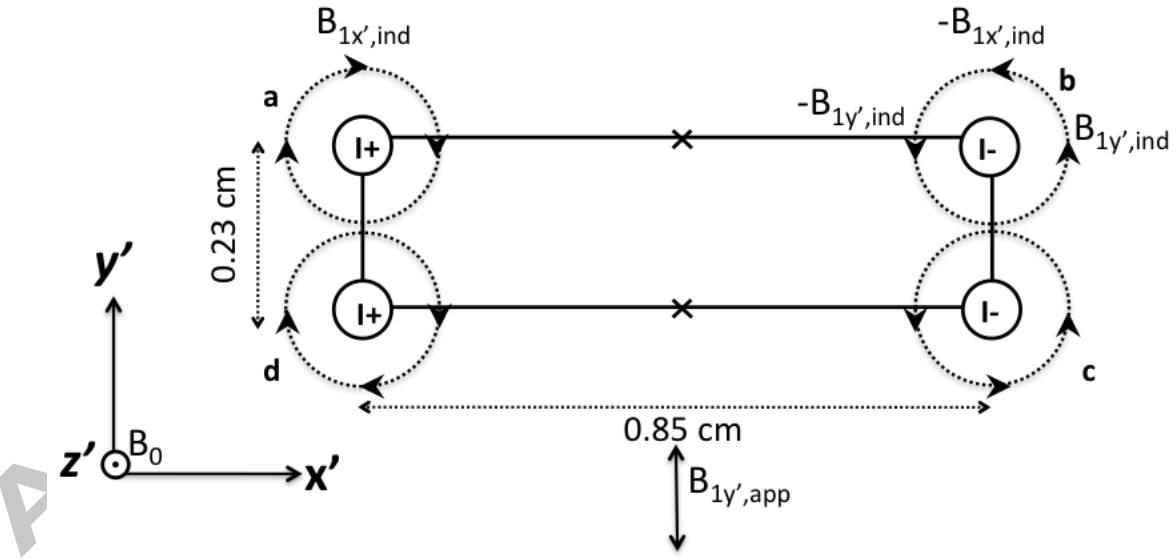

ACCEPTED MANUSCRIPT

Fig 5

(a) $H_{1x'}$

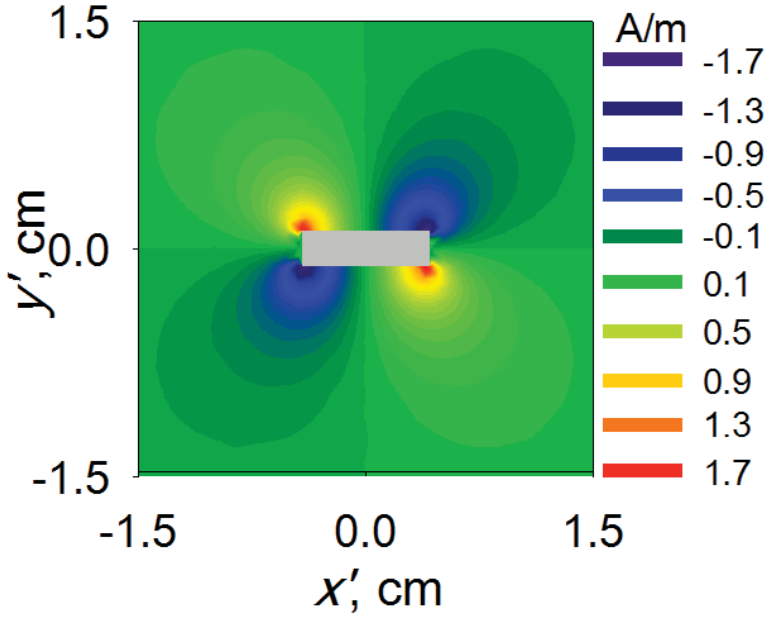

(b) $H_{1y'}$

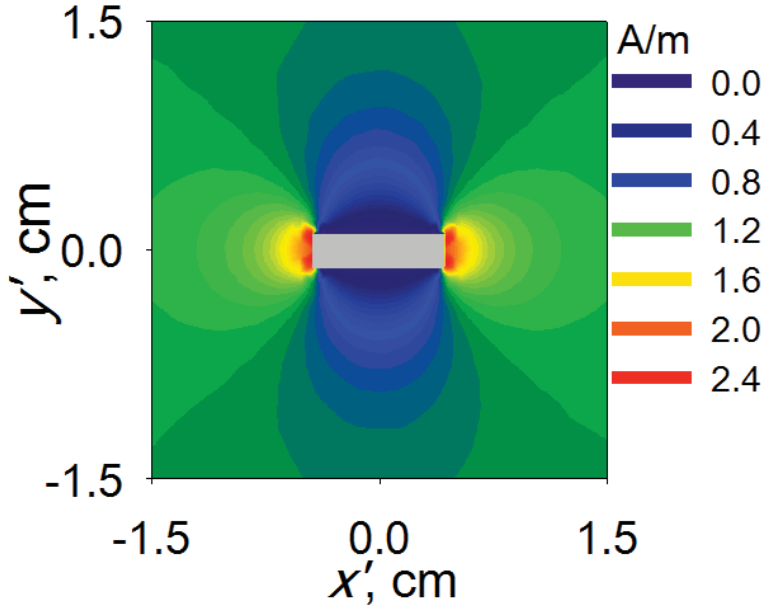

ACCEPTED MANUSCRIPT

Fig 6

(a)

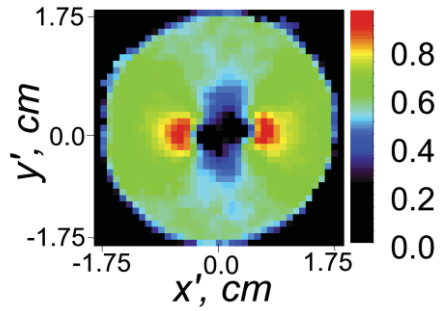

(b)

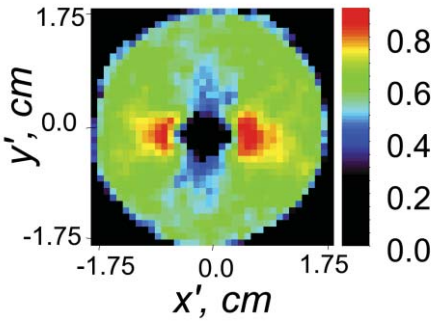

(c)

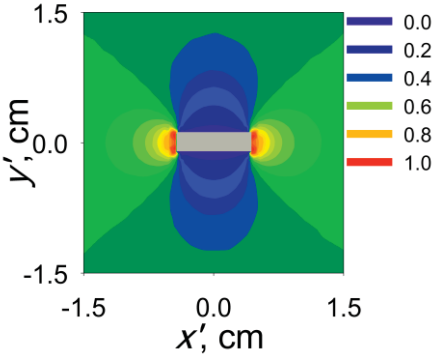

ACCEPTED MANUSCRIPT

Table 1.

	Good dielectric $\left(\frac{\sigma}{\omega\varepsilon}\right)^2 << 1$	Good conductor $\left(\frac{\sigma}{\omega\varepsilon}\right)^2 >> 1$
Attenuation constant, α	$\frac{\sigma}{2}\sqrt{\frac{\mu}{\varepsilon}}$	$\sqrt{\frac{\omega\mu\sigma}{\varepsilon}}$
Phase constant, β	$\omega\sqrt{\mu\varepsilon}$	$\sqrt{\frac{\omega\mu\sigma}{\varepsilon}}$

ACCEPTED MANUSCRIPT

ACCEPTED MANUSCRIPT

Table 2.

Parameters	Al	Pb
Conductivity, σ (S/m)	3.5×10^{7}	4.8×10^{6}
Relative Permeability, μ_r	1.00002	0.99998

ACCEPTED MANUSCRIPT

ACCEPTED MANUSCRIPT

References:

[1] M.M. Britton, P.M. Bayley, P.C. Howlett, A.J. Davenport, M. Forsyth, *In situ*, real-time visualization of electrochemistry using magnetic resonance imaging, J. Phys. Chem. Lett. 4 (2013) 3019-3023.

[2] Z. Zhang, J. Martin, J. Wu, H. Wang, K. Promislow, B.J. Balcom, Magnetic resonance imaging of water content across the Nafion membrane in an operational PEM fuel cell, J. Magn. Reson. 193 (2008) 259-266.

[3] R. Bhattacharyya, B. Key, H. Chen, A.S. Best, A.F. Hollenkamp, C.P. Grey, *In situ* NMR observation of the formation of metallic lithium microstructures in lithium batteries, Nature Materials 9 (2010) 504-510.

[4] L. Li. Q. Chen, A.E. Marble, L. Romero-Zeron, B. Newling, B.J. Balcom, Flow imaging of fluids in porous media by magnetization prepared centric-scan SPRITE, J. Magn. Reson. 197 (2009) 1–8.

[5] Q. Chen, B.J. Balcom, Measurement of rock core capillary pressure curves using a single-speed centrifuge and one dimensional magnetic resonance imaging, J. Chem. Phys. 122 (2005) 214720.

ACCEPTED MANUSCRIPT

ACCEPTED MANUSCRIPT

[6] Y. Zhao, Y. Song, T. Wang, Y. Liu, L. Jiang, N. Zhu, W. Yang Visualization of water flooding and subsequent supercritical CO_2 flooding in fractured porous media with permeability heterogeneity using MRI, Energy Procedia 37 (2013) 6942–6949.

[7] J.L.A. Williams, G. Maddinelli, D.G. Taylor, Selective magnetic resonance imaging of chemicals in sandstone cores during flow, J. Magn. Reson. 109 (1994) 124–128.

[8] M. Ouellette, H. Han, B. MacMillan, F. Goora, R. MacGregor, M. Hassan, B.J. Balcom, Design of a magnetic resonance imaging compatible metallic pressure vessel, J. Pres. Ves. Technol. 135 (2013) 045001-7.

[9] A.J. Ilott, S. Chandrashekar, A. Klöckner, H. Jung Chang , N.M. Trease, C.P. Grey, L. Greengard, A. Jerschow, Visualizing skin effects in conductors with MRI: Li MRI experiments and calculations, J. Magn. Reson. 245 (2014) 143-149.

[10] N. Augustiny, G.K. von Schulthess, D. Meler, P. Bosiger, MR imaging of large nonferromagnetic metallic implants at 1.5 T. J. Comput. Assist. Tomogr. 11 (1987) 678-683.

[11] J.S. Fache, C. Price, E.B. Hawbolt, D.K.B. Li, MR imaging artifacts produced by dental materials. Am. J. Neuroradiol. 8 (1987) 837-840.

ACCEPTED MANUSCRIPT

ACCEPTED MANUSCRIPT

[12] C.R. Camacho, D.B. Plewes, R.M. Henkelman, Nonsusceptibility artifacts due to metallic objects in MR imaging, J. Magn. Reson. Imaging 5 (1995) 75-88.

[13] L.H. Bennett, P.S. Wang, M.J. Donahue, Artifacts in magnetic resonance imaging from metals, J. Appl. Phys. 79 (1996) 4712-4714.

[14] A. Shenhav, H. Azhari, Gradient field switching as a source for artifacts in MR imaging of metallic stents, Magn. Reson. Med. 52 (2004) 1465-1468.

[15] U.A. Lauer, H. Graf, A. Berger, C.D. Claussen, F. Schick, Radio frequency versus susceptibility effects of small conductive implants: a systematic MRI study on aneurysm clips at 1.5 and 3 T, Magn. Reson. Imaging 23 (2005) 563-569.

[16] H. Graf, U.A. Lauer, A. Berger, F. Schick, RF artifacts caused by metallic implants or instruments which get more permanent at 3 T: an in vitro study, Magn. Reson. Imaging 23 (2005) 493-499.

[17] H. Graf, G. Steidle, U.A. Lauer, F. Schick, RF enhancement and shielding in MRI caused by conductive implants: dependence on electrical parameters for a tube model, Med. Phys. 32 (2005) 337-342.

ACCEPTED MANUSCRIPT

ACCEPTED MANUSCRIPT

[18] H. Graf. G. Steidle, P. Martirosian, U.A. Lauer, F. Schick, Effects on MRI due to altered RF Polarization near conductive implants or instruments. Med. Phys. 33 (2006) 124-127.

[19] S. Posse, W.P. Aue, Susceptibility artifacts in spin-echo and gradient-echo imaging. J. Magn. Reson. 88 (1990) 473-492.

[20] C.J.G. Bakker, R. Bhagwandien, M.A. Moerland, M. Fuderer, Susceptibility artifacts in 2DFT spin-echo and gradient-echo imaging: the cylinder model revisited, Magn. Reson. Imaging 11 (1993) 539-548.

[21] M. O'Donnell, W.A. Edelstein, NMR imaging in the presence of magnetic field inhomogeneities and gradient field nonlinearities, Med. Phys. 12 (1985) 20-26.

[22] A. Ericsson, A. Hemmingsson, B. Jung, G.O. Sperber, Calculation of MRI artifacts caused by static field disturbances. Phys. Med. Biol .10 (1988) 1103-1112.

[23] H. Imai, Y. Tanaka, N. Nomura, Y. Tsutsumi, H. Doi, Z. Kanno, K. Ohno, T. Ono, T. Hanawa, Three-dimensional quantification of susceptibility artifacts from various metals in magnetic resonance images, Acta. Biomater. 9 (2013) 8433-8439.

ACCEPTED MANUSCRIPT

ACCEPTED MANUSCRIPT

[24] J.K. Kim, D.B. Plewes, R.M. Henkelman, Phase constrained encoding (PACE): a technique for MRI in large static field inhomogeneities, Magn. Reson. Med. 33 (1995) 497-505.

[25] K. Sekihara, S. Matsui, H. Kohno, NMR imaging for magnets with large inhomogeneities. IEEE. Trans. Med. Imaging 4 (1985) 193-199.

[26] Z.H, Cho, D.J. Kim, Y.K. Kim, The total inhomogeneity correction including chemical shift and susceptibility by view angle tipping, Med. Phys. 15 (1988) 7-11.

[27] H. Chang, J.M. Fitzpatrick, A technique for accurate magnetic resonance imaging in the presence of field inhomogeneites, IEEE Trans. Med. Imaging 11 (1992) 319-329.

[28] F.G. Goora, H. Han, B.G. Colpitts, B.J. Balcom, Simulation and verification of magnetic field gradient waveforms in the presence of a metallic vessel in magnetic resonance imaging, IEEE Trans. Magn. 48 (2012) 2440-2448.

[29] F.G. Goora, H. Han, M. Ouellette, B.G. Colpitts, B.J. Balcom, Investigation of magnetic field gradient waveforms in the presence of a metallic vessel in magnetic resonance imaging through simulation, IEEE Trans. Magn. 49 (2013) 2920-2932.

ACCEPTED MANUSCRIPT

ACCEPTED MANUSCRIPT

[30] W.R. Nitz, A. Oppelt, W. Renz, C. Manke, M. Lenhart, J. Link, On the heating of linear conductive structures as guide wires and catheters in interventional MRI, J. Magn. Reson. Imaging 13 (2001) 105-114.

[31] K. El Banan, W. Handler, B. Chronik, S.P. Salisbury, Heating of metallic rods induced by time varying gradient field in MRI, J. Magn. Reson. Imaging 38 (2013) 411-416.

[32] H. Han, B. Balcom, Magnetic resonance imaging inside metallic vessels, Meas. Sci. Technol. 21 (2010) 1-5.

[33] H. Han, M. Ouellette, B. MacMillan, F.G. Goora, R. MacGregor, D. Green, B.J. Balcom, High pressure magnetic resonance imaging with metallic vessels, J. Magn. Reson. 213 (2011) 90-97.

[34] P. Stradiotti, A. Curti, G. Castellazzi, A. Zerbi, Metal-related artifacts in instrumented spine. Techniques for reducing artifacts in CT and MRI: state of the art, Eur. Spine. J. 18 (2009) 102-108.

[35] S. Gravina, D.G. Cory, Sensitivity and resolution of constant-time imaging, J. Magn. Reson. 104 (1994) 53-61.

[36] B.J. Balcom, R.P. MacGregor, S.D. Beya, D.P. Green, R.L. Armstrong, T.W. Bremner, Single-point ramped imaging with T_1 enhancement (SPRITE), J. Magn. Reson. 123 (1996) 131-134.

ACCEPTED MANUSCRIPT

ACCEPTED MANUSCRIPT

[37] M. Halse, D. J. Goodyear, B. MacMillan, P. Szomolanyi, D. Matheson, B.J. Balcom, Centric scan SPRITE magnetic resonance imaging, J. Magn. Reson. 165 (2003) 219-229.

[38] M.F. Lee, S. Kim, S.A. Lee, H.T. Song, Y.M. Huh, D.H. Kim, S.H. Han, J.S. Suh, Overcoming artifacts from metallic orthopedic implants at high-field-strength MR imaging and multidetecter CT: RadioGraphics 27 (2007) 791-803.

[39] M.J. Lee, D.L. Janzen, P.L. Munk, A. MacKay, Q.S. Xiang, A. MacGowen, Quantitative assessment of an MR technique for reducing metal artifact: application to spin-echo imaging in a phantom. Skeletal Radiol. 30 (2001) 398-401.

[40] H.G. Potter, B.J. Nestor, C.M. Sofka, S.T. Ho, L.E. Peters, E.A. Salyati, Magnetic resonance imaging after total hip arthoplasty: evaluation of periposthetic soft tissue, J. Bone Joint. Surg. Am. 86 (2004) 1947-1957.

[41] S. Vashaee, B. Newling, B. MacMillan, B.J. Balcom, B_1 mapping with a pure phase encode approach, J. Magn. Reson. 232 (2013) 68-75.

[42] C. A. Balanis, Advanced Engineering Electromagnetics. Reading Massachusetts Addison Wesley, Inc. USA, 1989.

ACCEPTED MANUSCRIPT

ACCEPTED MANUSCRIPT

[43] D.K. Cheng, Field and Wave Electromagnetics, second ed., Addison-Wesley , Inc. USA, 1989.

[44] E. Fukushima, S.B.W. Roeder, Experimental pulse NMR, Addison-Wesley, Massachusetts, USA, 1981.

[45] T. Weiland, Time domain electromagnetic field computation with finite difference methods, Int. J. Numer. Model. El. 9 (1996) 295-319.

ACCEPTED MANUSCRIPT

ACCEPTED MANUSCRIPT

Graphical abstract

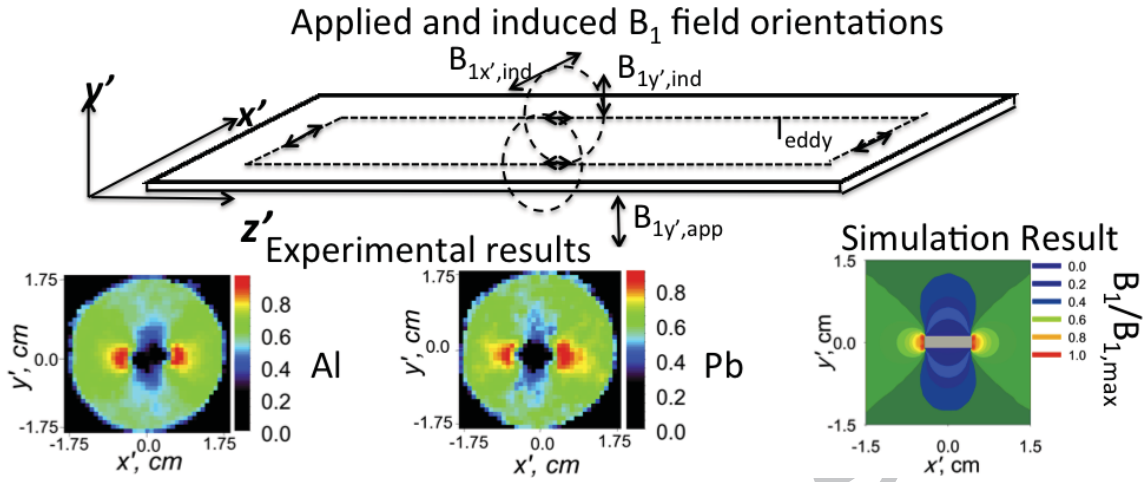

ACCEPTED MANUSCRIPT

ACCEPTED MANUSCRIPT

Highlights:

- RF induced MRI artifacts were investigated experimentally and by simulation
- We investigate artifacts by analyzing image distortions surrounding strip of metals
- The strip geometry was chosen to mimic electrode in electrochemistry studies
- The RF simulation results are in good agreement with experimental results

ACCEPTED MANUSCRIPT